Reliability Score Benchmarking and Resistive Loss Profile-Based Open-Circuit Fault Diagnosis Approach for Motor Drive System

Ali Arsalan, *Graduate Student Member, IEEE*, Behnaz Papari, *Senior Member, IEEE*, Laxman Timilsina, *Member, IEEE*, Grace Muriithi, *Graduate Student Member, IEEE*, Ali Moghassemi, *Graduate Student Member, IEEE*, SM Imrat Rahman, *Graduate Student Member, IEEE*, Elutunji Buraimoh, *Graduate Student Member, IEEE*, Gokhan Ozkan, *Senior Member, IEEE*, and Christopher S. Edrington, *Senior Member, IEEE*

***Abstract*—In recent years, data-driven methods have shown promise in diagnosing various open circuit fault (OCF) modes in inverter drive applications. However, existing studies primarily evaluate the reliability of these methods based solely on classification accuracy, neglecting critical real-time factors, such as computational delays and data transfer latency associated with the data-driven approach and communication protocols, respectively, which can affect real-time operational reliability. This article addresses these gaps by proposing a universally applicable reliability score criterion that integrates classification accuracy with system timing profiles. In addition, a model predictive control strategy employing active thermal management (ATM) is applied to the drive system, enabling a detailed analysis of the impact of OCF modes on the junction temperature of MOSFETs. Moreover, a novel feature extraction dataset is introduced, leveraging resistive/conduction loss data from the ATM scheme without requiring signal preprocessing. The proposed reliability score quantification and the dataset's diagnostic potential are validated using various data-driven classifiers. The most reliable classifier, achieving a 99.95% diagnosis accuracy, is further tested under diverse operating conditions using a control hardware-in-the-loop setup on an OPAL-RT testbed and Raspberry Pi.**

***Index Terms*—Active thermal management (ATM)-based model predictive control (MPC), online fault diagnosis, reliability score quantification, two-level three-phase inverter.**

I. Introduction

THREE-PHASE voltage source inverters (VSIs) have extensive applications in the automotive and electrical power sectors. Within these applications, open circuit faults (OCFs) in the power switches of VSI account for up to 38% of total inverter faults [1]. These faults pose significant challenges to a sustained system operation by causing extreme mechanical vibrations, electromagnetic torque distortions, and current fluctuations. This, in return, results in excessive thermal stress on healthy switches and subsequent failures of other adjacent system components. Therefore, various substantial methods for OCF diagnosis (detection and localization) are developed to ensure a reliable, safe, and continuous fault-tolerant operation of VSI. These methods can be broadly categorized as model-based, signal-based, and data-driven approaches [2].

In model-based fault diagnosis techniques, initially, an explicit mathematical model of the practical system is obtained by various observer-based approaches [3], [4], [5], parity equations [6], and state estimation schemes [7], [8]. Then, the model-generated outputs are compared to the actual measured values of the system for OCF diagnosis [2]. This approach offers a relatively fast diagnosis without any additional hardware. However, model-based schemes are not preferred due to the high dependence on the accuracy of the system model. This leads to problems associated with modeling complexity and parameter uncertainties in the working environment.

For signal-based schemes that do not use a system's mathematical model, fault indicators are identified by analyzing time or frequency domain signals using various signal processing techniques such as wavelet analysis and fast Fourier transform (FFT). These techniques, however, can increase the diagnostic time and computational burden [9] in signal-based methods. Moreover, these methods also suffer performance degradation due to load fluctuations and unbalanced operating conditions as well [2], [10]. Signal-based techniques can also be further divided into current-based [11], [12] and voltage-based [13], [14] methods based on the signal under test. In this regard, the current-based schemes have no extra hardware prerequisite and operate independently of converter parameters. Regarding diagnostic speed, current-based schemes require relatively more time, generally one fundamental period, to ensure higher detection accuracy, leading to slow diagnosis [15]. However, voltage-based methods exhibit better accuracy and higher diagnostic

Received 10 January 2025; accepted 23 February 2025. Date of publication 27 February 2025; date of current version 14 April 2025. This work was supported by the Clemson University's Virtual Prototyping of Autonomy Enabled Ground Systems (VIPR-GS), a US Army Center of Excellence for modeling and simulation of ground vehicles, under Grant W56HZV-21-2-0001 with the US Army DEVCOM Ground Vehicle Systems Center (GVSC). Recommended for publication by Associate Editor B. Akin. *(Corresponding author: Ali Arsalan)*

The authors are with the Secure Energy and Automation Laboratory (SEAL), and Real-Time Controls and Optimization Laboratory (RT-COOL), Clemson University, Clemson, SC 29634 USA (e-mail: aarsala@clemson.edu; bpapari@clemson.edu; ltimils@clemson.edu; gmuriit@clemson.edu; amoghas@clemson.edu; smimrar@clemson.edu; eburaim@clemson.edu; gokhano@clemson.edu; cedring@clemson.edu).

Color versions of one or more figures in this article are available at https://doi.org/10.1109/TPEL.2025.3546221.

Digital Object Identifier 10.1109/TPEL.2025.3546221

speed because the terminal voltage of power switches expresses the OCF features first compared to current-based methods [16]. Moreover, voltage-based techniques have complimentary hardware requirements, which, in return, increases the overall complexity of system topology, design cost, and sensor-based fault vulnerability points.

On the other hand, data-driven approaches can be applied to time-varying and complex nonlinear systems without relying on the system's model, pretuned thresholds, and load patterns. The limitation of data scarcity associated with this approach can be addressed by collecting the system's data in different operating conditions using reliable real-time simulators, such as OPAL-RT, Typhoon, and Speedgoat. Moreover, compared to the sturdy algorithms of signal-based and model-based methods, data-driven schemes exhibit high versatility and superior generalization performance, making this approach suitable for diagnosing various adjacent fault conditions in VSI.

Generally, data-driven methods use a data-based model to establish a mapping relationship, similar to system dynamics, between the input features and output labels [17]. Then, based on this correlation, the trained data-driven model is employed to distinguish between different system states. Moreover, a highly consistent, clean, correctly labeled and balanced data set can enhance the learning curve of a data-driven model. Therefore, various signal preprocessing techniques, such as FFT, principle component analysis (PCA), wavelet packet transform, and FFT+Relief, are used for input data dimensionality reduction and highly correlated feature extraction in [16], [18], [19], [20], [21], and [22]. These methodologies utilize random vector functional link (RVFL), Bayesian networks, multiclass relevance vector machine, long short-term memory (LSTM), and extreme learning machine (ELM)-based RVFL as OCF diagnosis algorithms for two-level and multilevel inverters. Apart from using frequency domain features, various time domain statistical features as diagnostic signals can also be used as in [23] and [24] with a data-driven classifier for abnormalities detection. Moreover, in [25] and [26], convolution neural network (CNN)-based fault diagnosis methods are proposed, where time-domain diagnostic signals are converted into 2-D images for OCF feature extraction. So, these feature extraction schemes can be categorized into frequency, time, and image-based approaches. Furthermore, in [27], various data-driven schemes have been evaluated for fault diagnosis in power electronics applications, showing that deep learning algorithms [i.e., LSTM, CNN, recurrent neural network (RNN), autoencoder] perform better than machine learning (ML) [i.e., support vector machine, ELM, decision tree (DT)] and neural network algorithms [i.e., multilayer perceptron (MLP), backpropagation neural network, radial basis function, and fuzzy neural network]. However, this proposition can vary based on the application.

The diagnostic speed of these data-based schemes relies heavily on feature extraction window size, data-driven model computational time, and data communication delay. In this regard, several past studies used the fixed window size to achieve balanced OCF diagnosis, as in [9], [16], [20], and [28], which is suitable for a motor drive system (MDS) with a short speed range. However, for a wide-speed domain, it can lead to inadequate or excessive diagnosis data, particularly when the fundamental period is significantly smaller or larger than the window size, which may result in misclassifications or slow diagnosis. Therefore, to overcome these shortcomings, a dynamic feature extraction time window as a function of the fundamental period is preferred in this work, where the input diagnostic data transfer rate will be proportional to the varying fundamental period of MDS.

Moreover, in existing data-based approaches, the diagnosis performance solely considers the predicted output and ground truth for accuracy evaluation during offline validation. Under this approach, a highly accurate data-driven classifier may work perfectly during online diagnosis when the sum of the computational latency of the data-driven model and communication delay is less than the feature extraction time-window size. However, at high RPMs with a fundamental period of a few milliseconds, the delay can exceed the window size, which may lead to congestion in the communication framework, overruns, slow diagnosis, and consistent false alarms. Hence, the conventional reliability quantification approach cannot guarantee the real-time diagnosis performance of a data-driven approach. Moreover, for a data-driven algorithm to work effectively, the sum of computational and communication delays should always be less than the feature extraction time-window size. Therefore, a data-driven approach with a simplistic feature extraction scheme and a data-driven classifier with less computational burden is always preferred. In this regard, various previously discussed data-driven schemes that use signal preprocessing techniques for feature extraction are exposed to high computational load. On the other hand, in the proposed scheme, the inherent segregation property of an ATM-based scheme is used as leverage to capture the dynamics of each semiconductor device in a three-phase inverter, which further acts as a reliable dataset for OCF diagnosis without the need for any signal preprocessing technique. So, the contributions of this work can be summarized as follows.

1) Existing data-based approaches typically use conventional classification accuracy as the primary reliability metric. However, this reliability score can demean at certain vulnerable instances, such as at high RPMs, during the real-time operation of MDS. To address this limitation, we propose a comprehensive reliability score that incorporates not only classification accuracy but also factors such as feature extraction time, model computation time, and data transfer delay, ensuring a more robust evaluation in realistic scenarios before online diagnosis.
2) The OCF is a single power switch can induce increased thermal stress on the healthy switches, which is rarely discussed in the existing literature. Therefore, this work also illustrates the real-time influence of various OCF modes on the junction temperature of power switches.
3) Combining data processing techniques, such as FFT with complex data-driven models can improve classification accuracy but often results in high computational costs [9]. To address this, this work introduces a simplified conduction loss profile-based dataset derived from ATM-based MPC as a novel OCF feature extraction method. This approach leverages predefined control layer signals, eliminating additional computational and hardware demands.

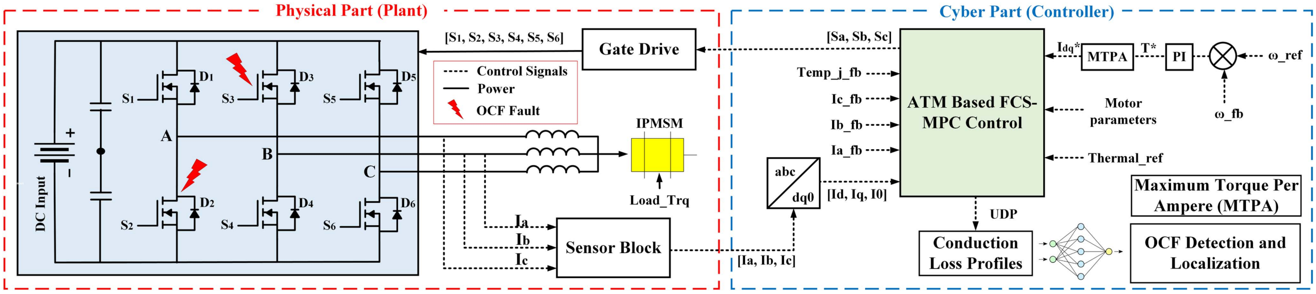

Fig. 1. Cyber–physical system of MDS based on ATM-based MPC.

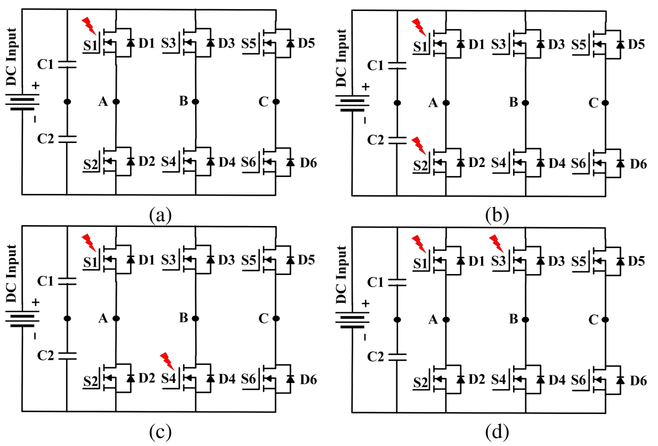

Fig. 2. Various OCF modes of inverter. (a) SS-OCF. (b) SDS-OCF. (c) CDS-OCF. (d) PDS-OCF.

TABLE I
LABELING VARIOUS OPERATION MODES OF INVERTER

Operation modes		Label	Operation modes		Label
Normal operation		0	CDS-OCF	S1, S4	10
				S2, S3	11
				S3, S6	12
SS-OCF	S1	1		S4, S5	13
	S2	2		S1, S6	14
	S3	3		S2, S5	15
	S4	4	PDS-OCF	S1, S3	16
	S5	5		S2, S4	17
	S6	6		S3, S5	18
SDS-OCF	S1, S2	7		S4, S6	19
	S3, S4	8		S1, S5	20
	S5, S6	9		S2, S6	21

TABLE II
CURRENT CONDUCTION SEQUENCE FOR MOSFETS AND DIODES IN PHASE-A UNDER VARIOUS OPERATING CONDITIONS

S_1 State	S_2 State	Current Direction	Conduction pattern (phase-A) S_1	S_2	D_1	D_2
ON	OFF	$i_a > 0$	Yes	No	No	No
ON	OFF	$i_a < 0$	No	No	Yes	No
OFF	ON	$i_a > 0$	No	No	No	Yes
OFF	ON	$i_a < 0$	No	Yes	No	No
OFF	OFF	$i_a > 0$	No	No	No	Yes
OFF	OFF	$i_a < 0$	No	No	Yes	No

Furthermore, the proposed dataset's effectiveness in OCF diagnosis is evaluated using a reliability score quantification scheme across various data-driven classifiers.

The rest of this article is organized as follows. Section III explains the MDS modeling with ATM-based MPC and conduction loss estimation. The proposed loss-based feature extraction dataset acquisition and reliability score formulation are elaborated in Section IV. Finally, Section V concludes this article.

II. SYSTEM LAYOUT AND FAULT LABELLING

The typical structure of the MDS with two-level, three-phase VSI is shown in Fig. 1. The control signals are generated via an ATM-based MPC, which considers the electrical and thermal attributes of a power converter for cost function minimization [29]. A simplified *RC* network known as a lumped parameter thermal network (LPTN) is used to model the thermal states of semiconductor devices analytically [29]. Moreover, the OCF associated with the inverter's semiconductor devices can mainly occur in single or two-power switches. Therefore, in this study, all possible combinations for single-switch and double-switch OCF are considered, which can be summarized as single-switch OCF (SS-OCF), series double-switch OCF (SDS-OCF), cross-double-switch OCF (CDS-OCF), and parallel double-switch OCF (PDS-OCF), as shown in Fig. 2 with different assigned labels in Table 1.

A. Conduction Loss Estimation

Each phase of a two-level, three-phase inverter consists of two power transistors (upper and lower) and two antiparallel diodes (upper and lower). The upper switch and lower diode can only conduct the positive current into machine winding, whereas the negative current can only flow through the upper diode and lower switch, as illustrated in Table 2. The power transistor and the diode conduct current consecutively in each switching period, as it can be correlated to Fig. 3(a), which shows the conduction losses of the upper power switch and lower diode during the positive half-cycle in normal mode. Moreover, conduction losses are influenced by several factors besides current values, including the switch brand and its associated ON-state resistance dynamics under varying junction temperatures and drain-to-source current values. This loss pattern almost remains the same for all the power transistors and the concerted diodes

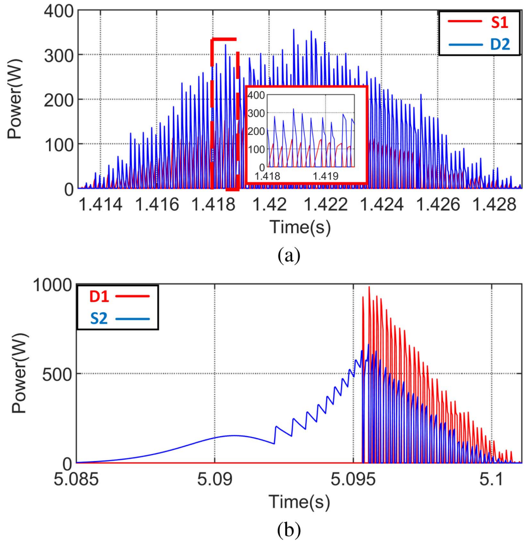

Fig. 3. Conduction losses in phase-A, (a) Normal operation. (b) Open-circuit fault.

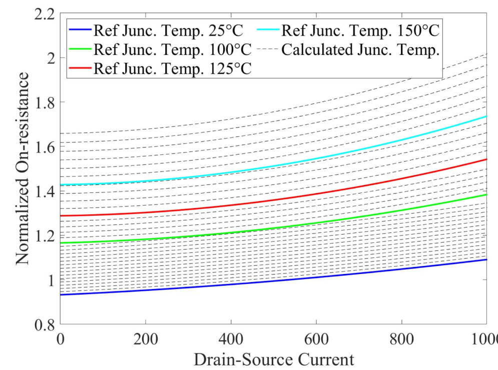

Fig. 4. Normalized ON-state resistance of SiC-MOSFET for different drain-to-source current and junction temperature.

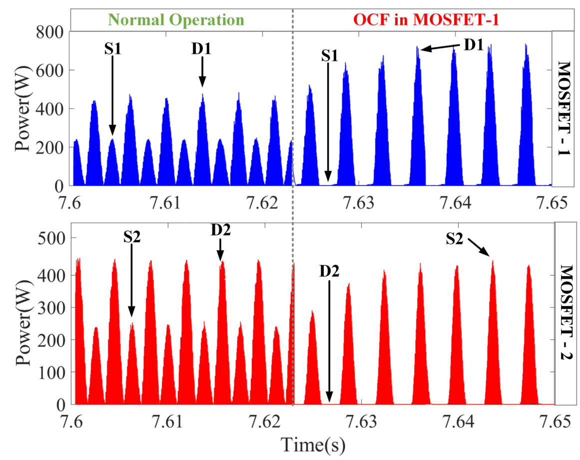

Fig. 5. Conduction loss in MOSFET-1 and MOSFET-2 during normal operation and OCF in MOSFET-1.

during normal operation. The power loss in the diode is higher than in the power transistor due to the larger weighted voltage drop during the forward bias condition. These weighted values are determined through curve fitting applied to the I_{ds} versus V_{ds} data provided in Fig. 7 of the SiC half-bridge module's datasheet (Cree/Wolfspeed CAB530M12BM3, 1200 V, 530 A) [30]. Similarly, the conduction losses for the power transistor are estimated using the relationship between I_{ds} and the normalized ON-state resistance of the MOSFET, as shown in Fig. 2 of the same datasheet. However, since the datasheet provides these values only for specific junction temperatures, the ON-state resistance for intermediate junction temperatures is calculated using the following approach:

$$R_{\text{ds(on)}}^{T_j} = R_{\text{ds(on)}}^{T_{j\,(\text{ref})}} \left(1 + \frac{\alpha}{100}\right)^{T_j - T_{j\,(\text{ref})}} \tag{1}$$

where T_j represents the junction temperature, $R_{\text{ds(on)}}^{T_{j\,(\text{ref})}}$ is the ON-state resistance at a predefined junction temperature (as specified in the datasheet), and α denotes the thermal factor, which is the rate of change of ON-state resistance with respect to the junction temperature. Using these parameters, $R_{\text{ds(on)}}^{T_j}$ refers to the ON-state resistance corresponding to the required junction temperature. The junction temperature, T_j, is calculated using the LPTN-based Cauer-type thermal network described in [29]. The calculated value of T_j is then used to estimate $R_{\text{ds(on)}}^{T_j}$ using (1), as illustrated by the dotted lines in Fig. 4. In addition, the current values for each MOSFET switch and diode under various switching states can be determined using the conduction pattern of phase-A, as shown in Table 2. Hence, the conduction losses for the MOSFET switch and diode can be formulated, as given in (2a) and (2b), respectively

$$P_{\text{cond}}^{\text{mft}} = I_{\text{ds}}^2 * R_{\text{ds(on)}}^{T_j} \tag{2a}$$

$$P_{\text{cond}}^{d} = I_F * V_F \tag{2b}$$

$$P_{\text{cond}}^{\text{total}} = P_{\text{cond}}^{\text{mft}} + P_{\text{cond}}^{d} \tag{2c}$$

where I_{ds} is drain-to-source current, and $R_{\text{ds(on)}}^{T_j}$ is obtained via (1). For (2b), I_F is the current flowing through the antiparallel diode, and V_F is the voltage drop across the diode under forward-bias condition. The total power loss for each of the semiconductor module per sampling period can be calculated by using (2c). Conduction losses vary significantly in the presence of OCFs in power transistors, resulting in distinct dynamic behaviors depending on the fault category. In this context, Fig. 3(b) illustrates the impact of conduction losses on D_1 and S_2 for a specific OCF case. The results show that the OCF influences the switching sequence, with S_2 remaining continuously ON for more than half of the negative half-cycle of phase A. This phenomenon is discussed in detail in the following section.

B. Conduction Loss Dynamics During OCFs

Fig. 5 shows the variation in conduction losses of power switches and antiparallel diodes in phase-A when OCF occurred in S_1. During normal operation, the conduction losses behave consecutively for each power switch and diode, where the diode has a higher loss value than the power switch. The total conduction losses for the power switch and diode in one cycle remain the same for both MOSFETs of each phase. Whereas, when

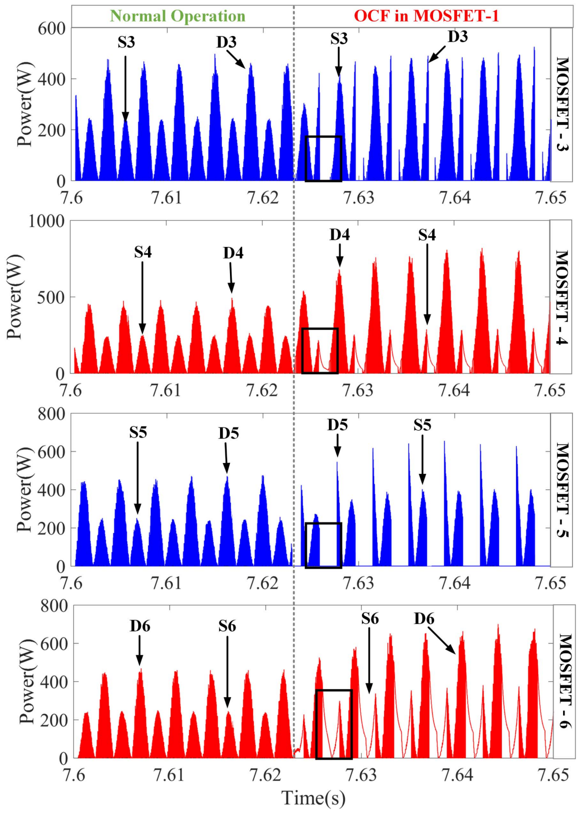

Fig. 6. Conduction loss in MOSFET-3, MOSFET-4, MOSFET-5, and MOSFET-6 during normal operation and under OCF in MOSFET-1.

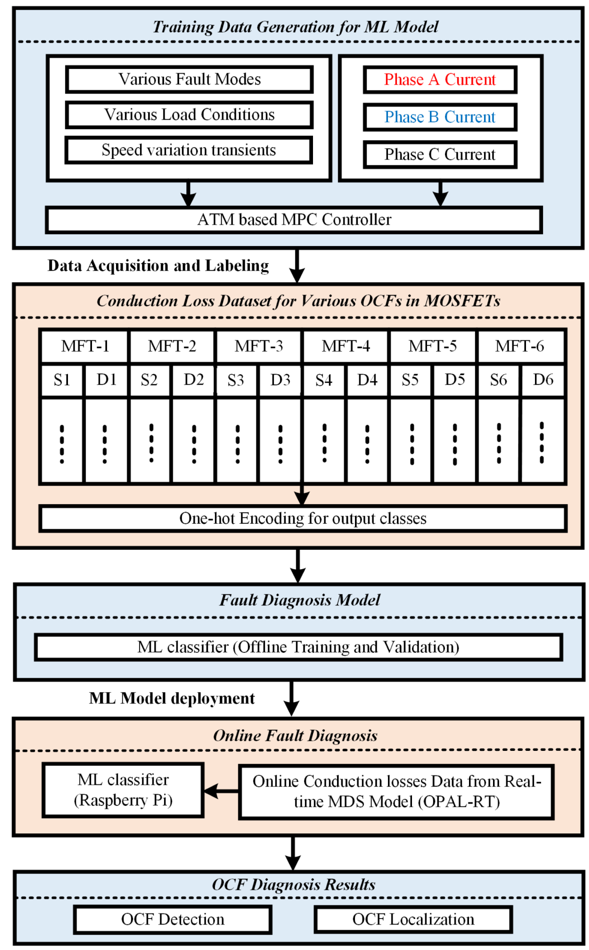

Fig. 7. Proposed conduction losses-based OCF diagnosis algorithm flowchart.

OCF occurred in S_1, the conduction loss for S_1 and D_2 turns to zero because conduction of the positive current of phase-A is no longer possible. Moreover, there is an increase in the conduction losses for D_1 and S_2 due to the associated rise in a negative current. Therefore, after the OCF in S_1, the total losses in one cycle for the upper MOSFET are higher because the diode conducts with inherently higher conduction losses. In addition, as these characteristics are independent of any triggering thresholds and load variations, they can be used as a reliable feature for fault diagnosis. When an SS-OCF occurs in one phase, the impact on frequency, magnitude, and phase also propagates to the remaining phases as well, which can be examined via FFT algorithm. In this regard, Fig. 6 shows the propagating impact of OCF in S_1, on the conduction losses for the remaining MOSFETs, in phases B and C. In Fig. 6, the highlighted instances where losses become zero are because of the MOSFET irregular behavior of continuous conduction controlled by switching states, also shown in detail in Fig. 3(b). Finally, these distortions in losses for all six semiconductor modules with distinct dynamics can be fed to train a data-driven algorithm for OCF diagnosis.

III. Proposed Method for OCF Detection and Localization

The proposed data-driven ML approach for an OCF diagnosis in a three-phase inverter, leveraging conduction losses as a key feature, is illustrated in Fig. 7. This approach involves two main stages: offline training of the ML network and its online deployment in a target environment for real-time OCF diagnosis.

Conduction losses serve as a highly effective feature for OCF detection and localization due to the inherent ability of the ATM-based MPC approach to segregate electrical losses, enabling optimal thermal stress control for each semiconductor device. The advantages of conduction losses over traditional three-phase current measurements for OCF diagnosis have been demonstrated in [31]. Unlike methods that rely on three-phase current combined with computationally intensive processes, such as FFT for fault frequency extraction and the ReliefF algorithm for feature selection and dimensionality reduction [16], conduction losses offer a more streamlined and efficient alternative. Since conduction loss dynamics are inherently generated within the ATM-based MPC framework, they require no additional computation beyond the MDS control layer.

This simplicity becomes particularly important when deploying ML classifiers in power electronics applications, where high computational loads can lead to overruns. An overrun occurs when the incoming data frequency from the MDS exceeds the processing speed of the ML network—resulting in slow diagnosis and potential false alarms. Therefore, it is crucial to consider the diagnostic data rate and the execution time of

ML classifiers during reliability testing and before real-time deployment of the model. To address these challenges, this work introduces a conduction loss-profile-based dataset as a new feature extraction approach and proposes a novel reliability quantification scheme for evaluating various ML classifiers in OCF diagnosis. These contributions ensure robust, real-time performance while minimizing computational overhead during deployment.

A. Feature Extraction and Preprocessing

The database, providing prior knowledge to an ML model about the operational characteristics of each MOSFET in an inverter, acts as a foundation to ensure the accuracy and reliability of the associated ML classifier. In this regard, 22 different operation modes of the inverter are considered, as given in Table 1. The operational data of MDS should be collected for each operation mode while considering various operating conditions associated with the reference speed and load torque of MDS. In this regard, for offline training, initially, the conduction losses of each power switch and diode, estimated via the three-phase output current of the inverter under various operating conditions, are obtained via (2a) and (2b)

$$\mathbf{X_{switch}} = \left[P^{\text{Loss}}_{s(i)}, P^{\text{Loss}}_{s(i+1)}, \ldots, P^{\text{Loss}}_{s(i+5)}\right], \quad i = 1 \tag{3}$$

$$\mathbf{X_{diode}} = \left[P^{\text{Loss}}_{d(i)}, P^{\text{Loss}}_{d(i+1)}, \ldots, P^{\text{Loss}}_{d(i+5)}\right], \quad i = 1 \tag{4}$$

where $P^{\text{Loss}}_{s(i)}$ and $P^{\text{Loss}}_{d(i)}$ represent the conduction losses in each power switch and antiparallel diode. These losses remain zero when there is no conduction, whereas, during the conduction cycle, loss values continuously switch between zero and nonzero values in each sampling instant, as shown in Fig. 3. The conduction cycle duration and the amplitude of conduction losses are influenced by the reference speed and load torque, respectively. Consequently, MDS operating under real-world conditions can exhibit rapidly changing and highly dynamic conduction loss behaviors, leading to unpredictable scenarios. These intricate inverter dynamics, involving all twelve semiconductor devices, demand more advanced ML models and larger training datasets. However, this approach significantly increases computational costs and adds complexity to the control architecture and data preparation process. Therefore, for OCF diagnosis, adopting a simplified dataset with a straightforward ML model offers several advantages. It enhances generalization, reduces computational and communication burdens, and improves the model's adaptability to handle unconventional or underrepresented scenarios efficiently. To address this, instead of considering the conduction loss value of each semiconductor device at every sampling period, the average conduction loss over a complete fundamental period is estimated. This preprocessing strategy simplifies the dataset while maintaining diagnostic effectiveness, given the data extraction window size of one fundamental period. The conduction loss transients in (3) and (4) are reformulated using this averaging approach, as outlined in the following:

$$T(t_c^s, t_c^d) = 2\pi/\omega_e \tag{5}$$

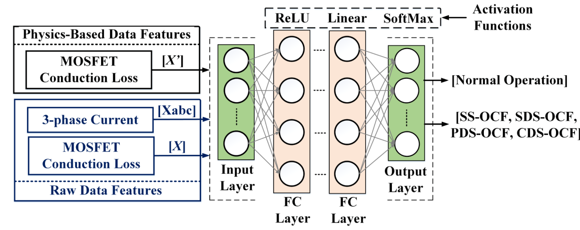

Fig. 8. Structure of feedforward MLP neural network used for multiclass classification.

$$X'_{(i)} = \begin{cases} \dfrac{\sum_{t=0}^{t_c^s} P^{\text{Loss}}_{s(i)}}{n_s^{(i)}}; & \forall\, P^{\text{Loss}}_{s(i)} > 0 \\ \dfrac{\sum_{t=0}^{t_c^d} P^{\text{Loss}}_{d(i)}}{n_d^{(i)}}; & \forall\, P^{\text{Loss}}_{d(i)} > 0 \end{cases} \tag{6}$$

$$i = \{1, 2, 3, 4, 5, 6\}$$

where T is the estimated fundamental time period, and ω_e is the electrical rotor speed (rad/s). Moreover, $X'_{(i)}$ represents the average values of conduction losses for the conduction period of each power switch and diode illustrated as t_c^s and t_c^d, respectively. In addition, $n_s^{(i)}$ and $n_d^{(i)}$ illustrate the total number of nonzero values in the conduction period of each power switch and diode, respectively. Furthermore, the effectiveness of various ML classifiers for the suggested OCF feature extraction method can be assessed using diverse performance metrics, such as accuracy, precision, and recall, as documented in the literature [32]. The architectures of the data-driven classifiers, including feedforward neural network (FNN) and LSTM, tested for the proposed OCF feature extraction method, are explained as follows.

B. Classification Using FNN

This study uses the most commonly used feedforward MLP neural network with four layers (one input, one output, and two hidden layers), as shown in Fig. 8. The input of an i_{th} neuron in the hidden layer without bias at nth learning instant can be defined as

$$\text{net}_i(n) = \sum_{j=1}^{J} m_{ij} x_j(n), \quad i = 1, 2, \ldots I - 1 \tag{7}$$

where J is the total number of neurons for the input layer, m is the weighting factor, and x_j is the input data from jth neuron. Moreover, a rectified linear unit activation function is applied to this sum of the first fully connected (FC) hidden layer as follows:

$$y_i(n) = \text{net}_i(n)^+ = \max(0, \text{net}_i(n))$$

$$y_i(n) = \begin{cases} \text{net}_i(n), & \text{if } \text{net}_i(n) > 0 \\ 0 & \text{otherwise.} \end{cases} \quad i = 1, 2, \ldots I - 1 \tag{8}$$

Finally, the sum of all hidden layer neuron outputs is fed into the output layer with the softmax activation function to predict the class labels. The output layer with softmax activation function transforms the output values from the FC layer into a

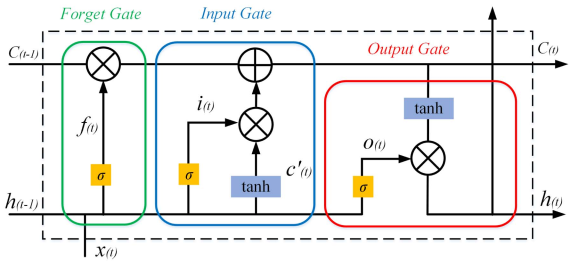

Fig. 9. Structure of a basic LSTM cell.

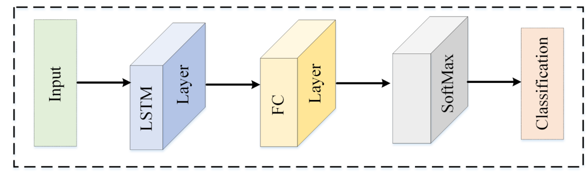

Fig. 10. LSTM-based neural network architecture.

probability distribution for all output classes, with the total sum equal to 1

$$\text{Softmax}(y_i(n)) = \hat{y}_i = \frac{e^{y_i(n)}}{\sum_{i=1}^{n_c} e^{x_i^{(n)}}} \tag{9}$$

where $y_i(n)$ represents the output from the FC layer's ith neuron at n learning sample, and n_c is the total number of target classes. Finally, the output from softmax is fed into the categorical cross-entropy cost function to minimize the error between predicted labels and ground truth while obtaining the optimal weights for hidden and output layers

$$\min J = H(y, \hat{y}) = -\sum_i y_i \cdot \log(\hat{y}_i) \tag{10}$$

where y_i and $\hat{y}_i$ represent the true (one-hot encoded) and the predicted probability of class i, respectively. The negative sign turns the cross-entropy minimization into a maximization problem. Backpropagation and gradient descent methods are used to adjust the weights and biases in FNN based on the cross-entropy error. Finally, Tensorflow is used to build this network with hyper-parameters as follows: batch size= 24, learning rate= 0.1 ms; 1 ms; 5 ms, hidden size = 16, optimizer = Adam.

C. Classification Using LSTM

An LSTM is the extended version of an RNN, preferred due to its ability to capture the long-term dynamic features and temporal patterns of sequential data. Therefore, similar to system dynamics, LSTM establishes a definitive correlation among different time series input features and better distinguishes between different system operational states. Hence, a correlation among time series data sets, similar to system dynamics, is established. Moreover, LSTM is computationally expensive and has a longer training time due to its complex architecture, as shown in Fig. 9, where the forget gate, input, and output gate are used to solve the vanishing gradient problem in conventional RNN and FNN. In addition, LSTM first calculates a candidate cell state $c'_{(t)}$ for the given input $x_{(t)}$ and output from the previous timestamp $h_{(t-1)}$, at each sampling period by using $c'_{(t)} = \tanh(m_h^c.h_{(t-1)} + m_x^c.x_{(t)})$. The forget gate, input gate, and output gate are calculated as follows [33]:

$$f_{(t)} = \sigma(m_h^f.h_{(t-1)} + m_x^f.x_{(t)}) \tag{11a}$$

$$i_{(t)} = \sigma(m_h^i.h_{(t-1)} + m_x^i.x_{(t)}) \tag{11b}$$

$$o_{(t)} = \sigma(m_h^o.h_{(t-1)} + m_x^o.x_{(t)}) \tag{11c}$$

where m_h^f, m_x^f, m_h^i, m_x^i, m_h^o, and m_x^o are the weights for each gate. Then, the new cell state $c_{(t)}$ and hidden state $h_{(t)}$ are computed by using $c_{(t)} = f_{(t)} \otimes c_{(t-1)} + i_{(t)} \otimes c'_{(t)}$ and $h_{(t)} = o_{(t)} \otimes \tanh(c_{(t)})$, respectively.

For the problem of diagnosing OCFs in an inverter, the architecture of the LSTM-based multiclass classifier used in this study is shown in Fig. 10. The network has a softmax layer to normalize the output predictions and a classification layer with a categorical cross-entropy cost function, as illustrated in (9) and (10). Moreover, Tensorflow is used to build this network with hyper-parameters as follows: batch size = 24, learning rate = 0.1 ms; 1 ms; 5 ms, hidden size = 16, optimizer = Adam.

D. Reliability Score Quantification

In most past studies, the applicability of ML models in power electronics applications is primarily centered on the ML network's accuracy, precision, and recall. However, incorporating ML-based networks with power electronics systems in real-world scenarios may pose constraints on system reliability arising from the computational burden associated with the ML model's complexity or their compatibility with the high diagnostic data rate from power converters. More specifically, the MDS, characterized by continuously changing fundamental periods, may result in overruns during communication with a complex ML model, specifically at high RPMs, thereby causing slow and unreliable diagnosis. Therefore, it is crucial to consider the timing profiles of these consecutive systems in the context of reliability evaluation before their real-world implementation. In this regard, system status trigger time ($t_{\text{tgr}}^{\text{ss}}$) and tolerance time ($T_{\text{tol}}$) is formulated as follows:

$$t_{\text{tgr}}^{\text{ss}} = \beta \cdot (T_{\text{fp}(r)}) + t_{\text{com}}^d + t_{\text{ex}}^{\text{ml}} \tag{12a}$$

$$T_{\text{tol}} = \delta \cdot (T_{\text{fp}(r)}) \tag{12b}$$

where $t_{\text{tgr}}^{\text{ss}}$ is the time taken to produce the associated operational label of the inverter, mentioned in Table 1. Furthermore, $T_{\text{fp}(r)}$ denotes the fundamental time period at the rated speed of MDS. t_{com}^d represents the communication delay during two-way data transmission between MDS and ML-model, and $t_{\text{ex}}^{\text{ml}}$ signifies the execution time of ML-model to process a singular set of data for predicting an output class. Moreover, the first term of (12a) represents the proportion of $T_{\text{fp}}(r)$ used for data accumulation before it is transmitted to the ML model. The value of the weighting factor β depends on the design parameters of the proposed approach, where the time-window size for feature extraction is the function of the fundamental period. Generally, it is always preferred to have an β as small as possible to have a fast OCF detection without compromising optimal OCF diagnosis performance. Nevertheless, some past studies have preferred fixed window size to achieve balanced diagnosis time, as in [16]. This approach, however, can lead to inadequate OCF feature data or a slow diagnosis process at some instances of speed. Anyhow, for the reliability quantification of the approach with fixed window size, the first term of (12a) will be replaced with the associated time window value. In addition, T_{tol} signifies the critical remaining lifetime before an OCF in a MOSFET inflicts permanent damage to MDS's adjacent components due to accelerated aging and increased thermal stress [34], [35]. This critical time can also calculated by using the degradation forecasting approach, which can be a promising area of research for our future work. However, in this proposed study, T_{tol} is defined as a function of $T_{\text{fp}(r)}$ and the scaling factor δ, which is assumed to be equal to 10. For an MDS operating at a maximum speed of 733.04 rad/s (US06 drive cycle maximum speed), the fundamental period is 2.14 ms. At this speed, fault conditions would persist for roughly ten fundamental periods before existing diagnostic schemes [9], [16], [19], [36], with an average feature extraction window of approximately 25 ms, detect the OCF. For lower speeds, the fundamental period will be longer, and hence the fault conditions will persist for fewer fundamental periods. Therefore, we considered the maximum speed as it provides the maximum threshold of the number of cycles we can tolerate under faulty conditions. Hence, we chose $\delta = 10$ as a practical and conservative assumption, reflecting a reasonable weighting factor for the tolerance time estimation, based on prior research insights. Moreover, in terms of reliability quantification, T_{tol} provides an upper bound for the detection time, i.e., the lesser the value of $t_{\text{tgr}}^{\text{ss}}$ compared to T_{tol}, the better the reliability. Finally, the accumulated classification efficiency of the ML model, using conventional gauging parameters, is given as

$$\eta_{\text{ml}} = \frac{A + P_m^{\text{avg}} + P_w^{\text{avg}} + R_m^{\text{avg}} + R_w^{\text{avg}} + F1_m^{\text{avg}} + F1_w^{\text{avg}}}{7} \tag{13}$$

where A denotes accuracy, while P_m^{avg}, R_m^{avg}, $F1_m^{\text{avg}}$, P_w^{avg}, R_w^{avg}, $F1_w^{\text{avg}}$ indicate the macroaverage values and weighted-average values of precision, recall, and F1 score, respectively. Moreover, during the training of the ML model, it is ensured that any individual output class value for precision, recall, and F1 score is not completely zero. Finally, the reliability score of an ML model based on the timing profile and the conventional efficiency scoring mechanism is developed as follows:

$$R_s = \psi_{(T_{\text{tol}})} \left[\frac{\left(1 - \frac{t_{\text{tgr}}^{\text{ss}}}{T_{\text{tol}}}\right) + \psi_{(T_{\text{fd}}^{\min})} \left(1 - \frac{t_{\text{com}}^{\text{d}} + t_{\text{ex}}^{\text{ml}}}{T_{\text{fd}}^{\min}}\right) + \eta_{\text{ml}}}{3} \right] \tag{14}$$

where $\psi_{(T_{\text{tol}}), T_{\text{fd}}^{\min})} \in \{0, 1\}$ represents a bipolar parameter. $\psi_{(T_{\text{tol}})}$ assumes the value of zero if $t_{\text{tgr}}^{\text{ss}} > T_{\text{tol}}$ and $\psi_{(T_{\text{fd}}^{\min})}$ will be zero if $(t_{\text{com}}^{\text{d}} + t_{\text{ex}}^{\text{ml}}) > T_{\text{fd}}^{\min}$; otherwise, they take the value of one. Moreover, this proposed OCF diagnosis approach uses a dynamic window size associated with a fundamental period for OCF feature extraction. Therefore, $T_{\text{fd}}^{\min}$ as the most vulnerable

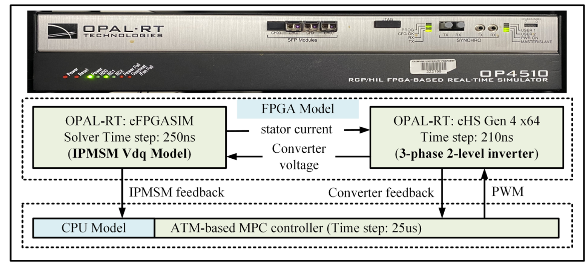

Fig. 11. MDS with ATM-based MPC control implementation on OPAL-RT testbed.

instance is used in (14), which indicates the minimum fundamental period (which will be at highest possible RPM) for a three-phase inverter output current. This period is considered the most vulnerable because it has the highest possible diagnostic data transfer rate from MDS to the ML model and is highly susceptible to overruns. Hence, evaluating the system under its most vulnerable conditions is crucial to achieving a practically feasible reliability assessment. Moreover, for the reliability quantification for the fixed window size scheme, the $T_{\text{fd}}^{\min}$ value will be replaced with the associated feature extraction time window value.

IV. Real-Time Experimental Validation

The performance of the proposed OCF diagnosis approach is demonstrated through a real-time CHIL platform setup carried out on an MDS, shown in Fig. 1. This CHIL experiment aims to illustrate the viability of the presented framework for real-time applications. Moreover, the subsequent section explains the implementation steps and experimental results for this real-time experiment.

A. System Modeling

The MDS with ATM-based MPC is implemented in MATLAB/Simulink environment integrated with the real-time digital simulator, i.e., Opal-RT OP4510. The model is executed in RT-LAB with real-time hardware synchronization mode. Moreover, the detailed implementation of MDS in OPAL-RT is shown in Fig. 11, where the power converter and PMSM are simulated in the FPGA solver with a sampling time of up to 210 ns, and the controller is implemented in the CPU of OPAL-RT with a sampling rate of 25 μs. The OCFs in different power switches of the inverter are instigated by disabling the gate drive signals from the console subsystem in the real-time MDS model, as shown in Fig. 12.

Python-based scripts, such as ML multiclass classifiers, are implemented on Raspberry Pi 4 model B, which aims to detect and localize OCFs in power converter, as described in Section IV. Moreover, for real-time OCF location visualization, a GUI is also modeled in Raspberry Pi using the Tkinter interface, illustrating each MOSFET's normal or OCF status in the power converter. The OPAL-RT and Raspberry Pi are linked via user datagram protocol (UDP). The real-time values of conduction losses from the control layer of the MDS model (i.e., OPAL-RT) are transmitted to Raspberry Pi, where an ML-based OCF

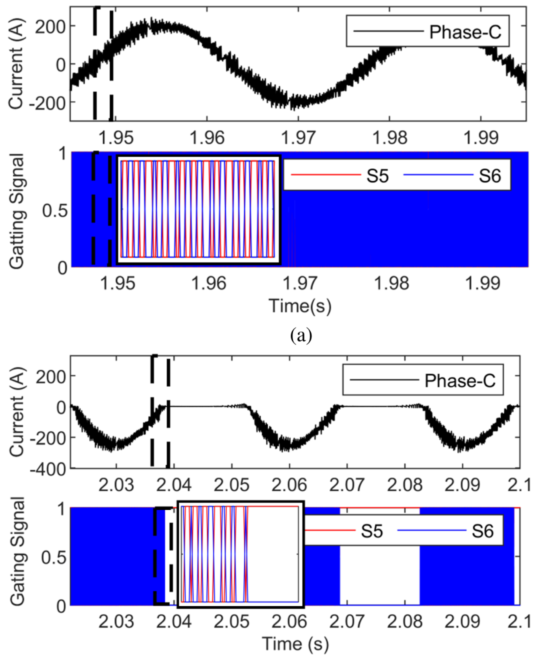

Fig. 12. Current waveform and gating signals variation during different modes of operation. (a) Normal operation. (b) SS-OCF.

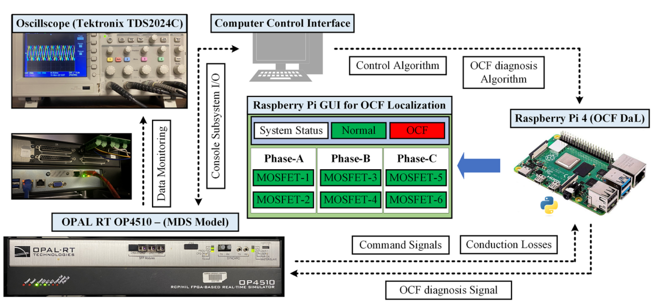

Fig. 13. CHIL experimental setup for real-time OCF diagnosis.

diagnosis algorithm runs to predict output class labels based on Table 1. Finally, depending upon the predicted label, the operational status of each MOSFET is represented in the GUI, and an OCF diagnosis signal is also sent back to the OPAL-RT for data monitoring on the oscilloscope. The detailed layout of the proposed strategy via the CHIL experiment setup is shown in Fig. 13.

Moreover, to efficiently utilize the available computation resources, the OCF diagnosis algorithm uses multithreading by concurrently running three threads (utilizing three out of four cores in Raspberry Pi). The first thread realizes the communication protocol to exchange the OCF trigger and input diagnosis data between connected nodes, while the second thread runs an ML-based OCF diagnosis neural network, generating the OCF DaL signals to be sent back to OPAL-RT by leveraging the same communication protocol implemented in the first thread. Moreover, the GUI is deployed in the third threat, which receives each MOSFET's health status signal from the second thread.

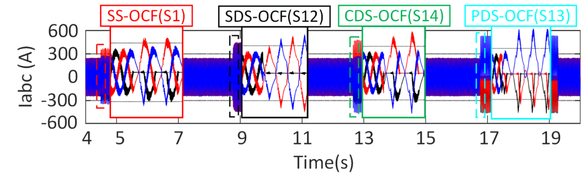

Fig. 14. Inverter output current dynamics during different OCFs.

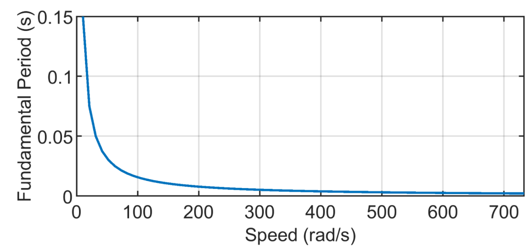

Fig. 15. Fundamental time period variation for a range of reference speed.

B. Conduction Loss-Based Real-Time Data Acquisition

To validate the performance and reliability of the proposed ML approach for OCF diagnosis under real-time system dynamics, training data is gathered for various operating conditions from the OPAL-RT-based MDS model illustrated in Fig. 11. In this regard, various categories of single and double-switch OCFs are instigated, as illustrated in Fig. 14. Moreover, the reference speed is varied between 20 rad/s to 200 rad/s with an interval of 20 rad/s. This period is considered due to substantial change in the fundamental period, as shown in Fig. 15. Moreover, the data associated with conduction losses of each power switch and diode for different operating modes (mentioned in Table 1) is obtained at each incremented interval of reference speed. In this regard, Figs. 16 and 17 show the real-time plots of conduction losses of phases A, B, and C for single, cross, series and parallel-switch OCFs. During normal operation, the losses of all the diodes are always higher than those of their associated power switches. However, this proposition can vary after an OCF is instigated at the time (t_{oc}). The variations in these loss values are associated with the impacted switching sequence of power switches after t_{oc}. Each type of OCF has a different impact on these losses, which can be quantified by the ATM approach discussed in [29]. Moreover, OCF in a power switch turns conduction losses to zero for that switch and its associated diode in the same phase, which is true for all OCF modes. Hence, this real-time data associated with each semiconductor device during various operating states of MDS is collected and further used for OCF feature extraction, as explained in Section IV. Furthermore, the MDS can have a wide speed profile of up to approx. 733.04 rad/s (observed in US06 drive cycle), with a fundamental period varying between 150 and 2.14 ms, as shown in Fig. 15, particularly in EV applications. So, using a fixed time window for feature extraction in a frequency-varying system can lead to slow diagnosis and misclassifications due to abnormalities in extracted feature data. Moreover, computing an optimal value of time-window size for a balanced diagnosis in a wide-speed MDS profile can also be very challenging. Conversely, the

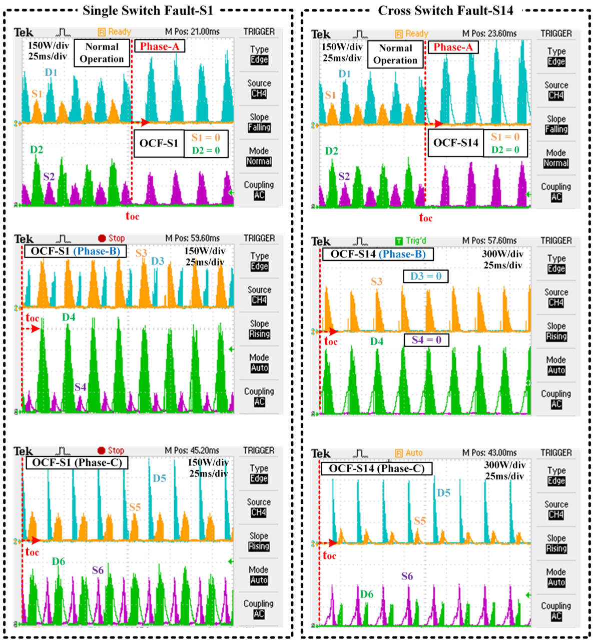

(a) (b)

Fig. 16. Effect of OCFs on conduction losses for phases A, B, and C. (a) SS-OCF. (b) CDS-OCF.

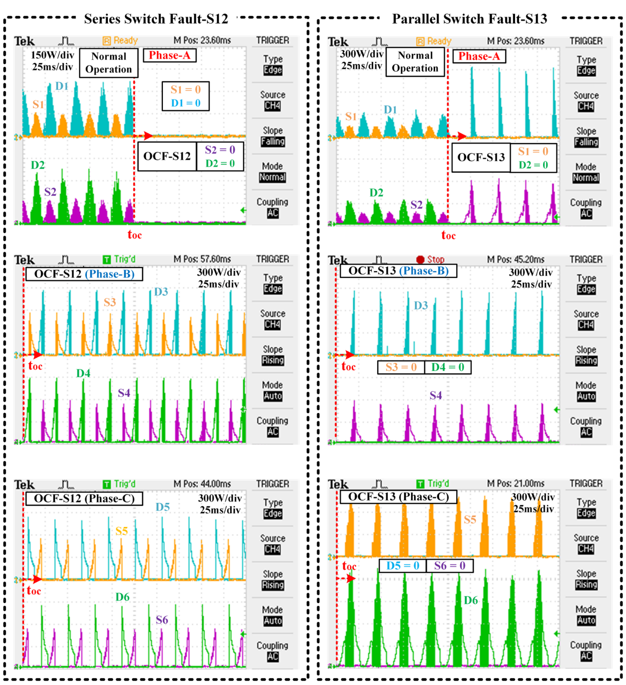

(a) (b)

Fig. 17. Effect of OCFs on conduction losses for phases A, B, and C. (a) SDS-OCF. (b) PDS-OCF.

fundamental period-based time window approach is much more simplistic and can achieve fast diagnosis at high RPMs when the system is highly susceptible to physical faults. However, for this approach to work perfectly, it is crucial to consider the timing profiles of the data-based approach for reliability score quantification.

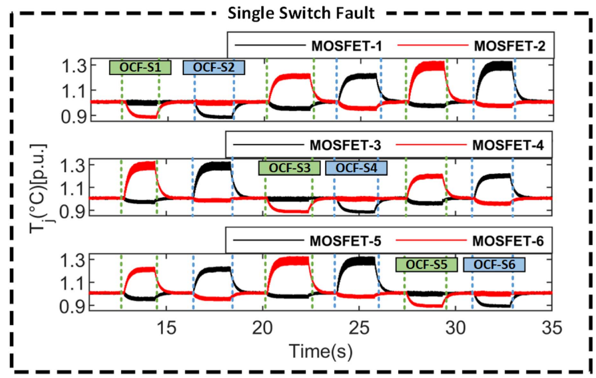

(a)

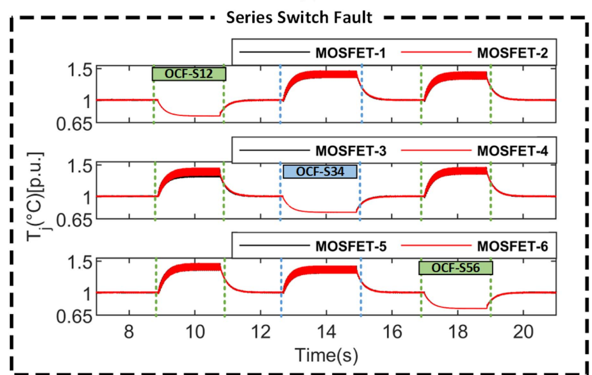

(b)

Fig. 18. Thermal imbalance among MOSFETs and increased thermal stress due to various OCF scenarios. (a) SS-OCF. (b) SDS-OCF.

C. Impact of Different OCFs on MOSFET Junction Temperature

The current distortion with magnitude and phase variations caused by various OCFs can accelerate the aging and the thermal stress for some semiconductor devices in an inverter. This rise in temperature is considered a salient feature in measuring the health condition of a MOSFET because most electrical faults ultimately reflect damage in the form of increased thermal stress. Therefore, it is very meaningful to study the thermal impact of various OCFs on MOSFETs to model better thermal control schemes. So, different single and double-switch OCFs mentioned in Table 1 are instigated in the real-time model of the MDS shown in Fig. 11. The real-time effect of each category of OCFs on the three-phase output current can also be seen in Fig. 14. Moreover, the impact on each MOSFET's junction temperature (T_j) due to SS-OCFs in all six power switches is shown in Fig. 18(a). During normal operation, the T_j for each MOSFET remains the same. However, when an SS-OCF is instigated, the T_j does not show any substantial variation for MOSFET under fault, whereas the other MOSFET in the same phase experiences a decline in T_j. This decline is because this T_j is associated with the lower losses of the power transistor. Meanwhile, the higher T_j of MOSFET under fault is because this T_j is associated with the higher losses of the antiparallel diode. Moreover, It can also be concluded by Fig. 18(a) that SS-OCF in the upper switch of a phase has a higher impact on the T_j of the lower MOSFETs of the other two phases compared to the upper switches

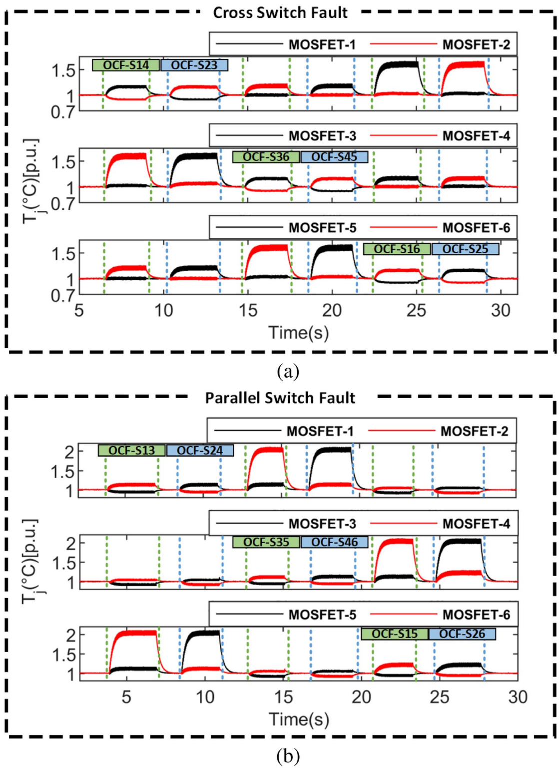

Fig. 19. Thermal imbalance among MOSFETs and increased thermal stress due to various OCF scenarios. (a) CDS-OCF. (b) PDS-OCF.

and vice versa. In addition, for MOSFETs under SDS-OCF, the T_j drops to ambient temperature for both MOSFETs in all three cases, as shown in Fig. 18(b). Meanwhile, the MOSFETs in the remaining two phases without fault experience a similar rise in T_j. Moreover, compared with SS-OCF, SDS-OCF puts higher thermal stress on the T_j of MOSFETs without fault.

In addition, Fig. 19 explains the impact of various CDS-OCFs and PDS-OCFs on T_j of MOSFETs. In the case of CDS-OCFs, the MOSFET with a power switch under fault has a higher T_j than the other MOSFET in the same phase, similar to SS-OCF. These higher T_j are normally associated with the conduction losses of diodes having a higher area under the curve. Moreover, in the case of all double-switch CDS faults, the latter switch, such as $S4$ in the case of OCF-S14, always has a higher impact on T_j, as shown in Fig. 19(a). This shows the uneven current distribution among MOSFETs due to OCFs, whereas, in normal operation, the current is always balanced. Moreover, in the case of PDS-OCF, it can be seen in Fig. 19(b) that the lower MOSFET of the phase without fault has the highest T_j when the upper two switches of the remaining phases are under OCF and vice versa. This is because, in the case of PDS-OCF, the controller always tries to avoid the scenario where all top or bottom MOSFETs are OFF. Due to PDS-OCF, either the top two or bottom two MOSFETs of two-phase are under OCF; if the third parallel MOSFET also goes into OFF condition, then the output of the inverter will be zero, hence maximizing the MPC cost function. Finally, comparing all four categories of OCFs shows that the PDS-OCF propagates the highest thermal impact on the MOSFET without fault. In addition to the uneven thermal stress distribution among switches caused by OCFs, Fig. 20 illustrates the elevated thermal stress in the form of increased thermal cycling, as highlighted using a box plot for the MOSFETs in phase-A under a specific OCF scenario. The figure demonstrates not only the rise in junction temperature due to the OCF but also the increased variation/spread in junction temperature after reaching its peak values, indicating intensified thermal cycling effects. Thus, this thermal impact quantification can further be used for the degradation forecasting of healthy MOSFETs due to OCFs and lead to critical time estimation mentioned in (12b).

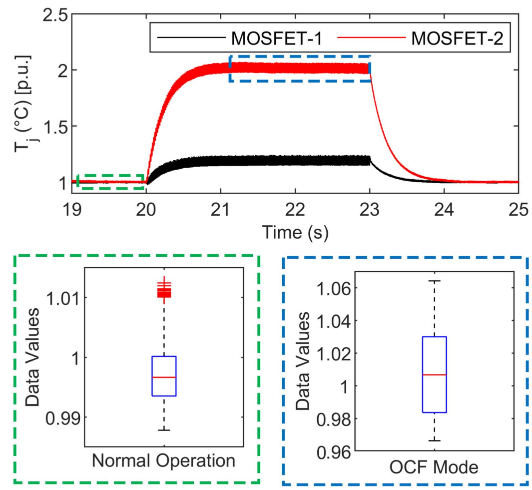

Fig. 20. Increased thermal stress characterized by heightened thermal cycling under OCF scenario.

D. Offline Validation

The obtained MDS data is split into training and testing data sets with a 70:30 ratio for the training and evaluation of various state-of-the-art ML networks. These networks' frameworks are then optimized to achieve fast convergence using hit and trail on various hyperparameters, including batch normalization, dropout layers, number of hidden layers and neurons, batch size, and learning rate. Moreover, the ML network structures are kept as simplistic as possible to reduce the computational burden while avoiding overfitting or underfitting issues. The architecture of these neural networks is already explained in Section IV. Moreover, the validity of the proposed OCF feature extraction approach for various ML classifiers, including FNN, LSTM, random forest (RF), and DT, is illustrated in Table 3. In this regard, Fig. 21 signifies the convergence rate of accuracy for FNN and LSTM neural networks, considering different learning rates for one hundred epochs, with FNN showing better accuracy and rapid convergence. A higher learning rate is preferred as it can lead to fast training; However, it can also cause convergence issues. Furthermore, comparing the accuracy of all ML classifiers in Table 3, FNN has the highest value for training and testing datasets. Whereas, in the case of training time, DT has the least duration with a value of 0.067 s.

TABLE III
PERFORMANCE COMPARISON AMONG VARIOUS ML CLASSIFIERS

ML classifier	Characteristics	Learning rate (Δt)			Reliability score quantification	
		0.1 ms	**1 ms**	**5 ms**	$\mathbf{t_{ex}^{ml}}$ **(ms)**	$\mathbf{R_s}$**(%)**
FNN	Accuracy	[99.88, 99.88]	[100, 100]	**[100, 100]**	**0.6**	**77.31**
	Training time (s)	39.14	14.6	**5.18**		
	Epoch	100	40	14		
LSTM	Accuracy	[94.01,93.94]	[98.59,98.55]	[98.59, 98.45]	1.9	60.59
	Training time (s)	268.05	268.22	268.82		
	Epoch	100	100	100		
RF	Accuracy	[100, 100], (No. of trees = 3)			7.0	56.39
	Training time (s)	0.214, (No. of trees = 3)				
	Accuracy	[100, 99.92], (No. of trees = 2)			5.9	57.21
	Training time (s)	0.167, (No. of trees = 2)				
DT	Accuracy	[100, 99.83]			0.9	71.98
	Training time (s)	0.067				

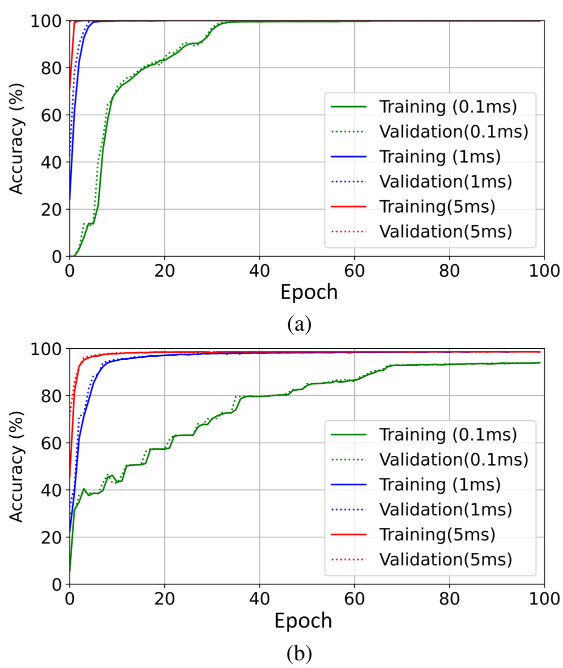

Fig. 21. Accuracy curves for two neural networks. (a) FNN. (b) LSTM.

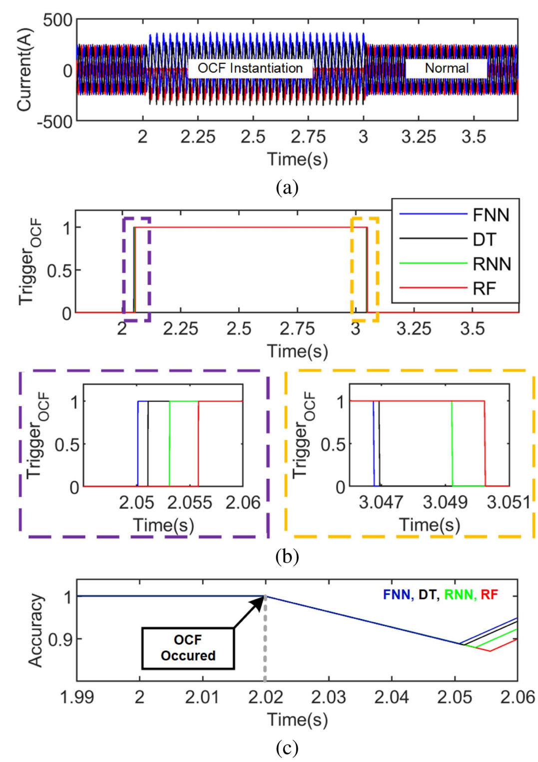

Fig. 22. Real-time OCF diagnosis for different ML classifiers. (a) Three-phase current under OCF-S1. (b) OCF diagnosis time. (c) Accuracy dip.

E. Real-Time Reliability Analysis

Moreover, various reliability score parameters derived from real-time testing are also mentioned in Table 3. In this regard, t_{ex}^{ml} is obtained by running each trained ML classifier in Raspberry Pi for a single input data frame. As a result, FNN signifies the least computational burden, whereas t_{ex}^{ml} of RF shows the highest execution time of 7.0 ms. Furthermore, when t_{ex}^{ml} is compared to T_{fd}^{min}, i.e., 2.14 ms, FNN and DT are prone to illustrate superior computational performance in terms of overruns compared to LSTM and RF. Moreover, during the actual implementation of such diagnosis approaches, the delay associated with the communication framework must also be considered. In this regard, Fig. 22 shows the real-time detection of an SS-OCF in S1 based on the proposed OCF feature extraction approach with communication and computational latency during data transmission between OPAL-RT and Raspberry Pi. The communication delay is not always fixed due to the dynamic nature of the communication network, as shown in Fig. 22(b), where the diagnosis delay for four different ML classifiers is compared. The detection sequence based on t_{ex}^{ml} remains the same, with FNN showing the least OCF diagnosis time of approx. 1.0 ms.

These different diagnosis periods are primarily associated with t_{ex}^{ml}, and the bidirectional data transfer delay for the UDP framework used in the experimental testbed, which is approx. 0.5 ms. This value is obtained via various data-transfer loopback tests between OPAL-RT and Raspberry Pi. The delay can vary for other communication protocols, such as transmission control protocol, control area network buses, FlexRay communication, and local interconnect network. Moreover, Fig. 22(c) shows the

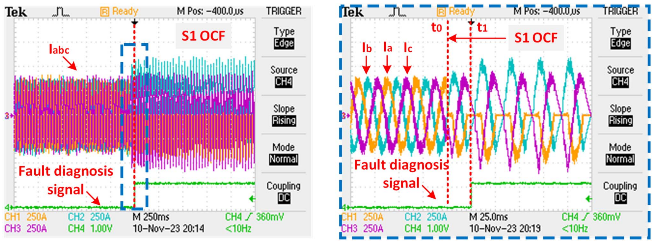

Fig. 23. CHIL OCF diagnosis results for an SS-OCF.

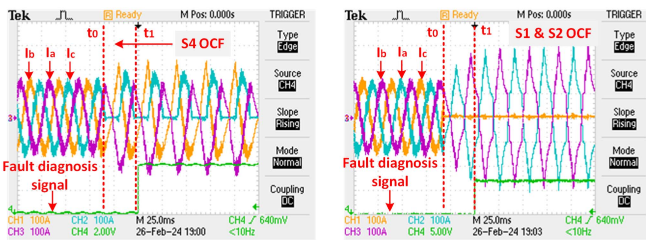

(a) (b)

Fig. 24. CHIL OCF diagnosis results. (a) SS-OCF. (b) SDS-OCF.

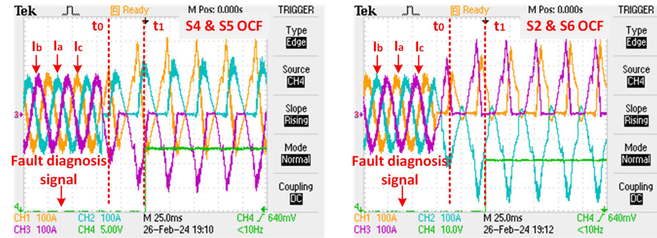

(a) (b)

Fig. 25. CHIL OCF diagnosis results. (a) CDS-OCF. (b) PDS-OCF.

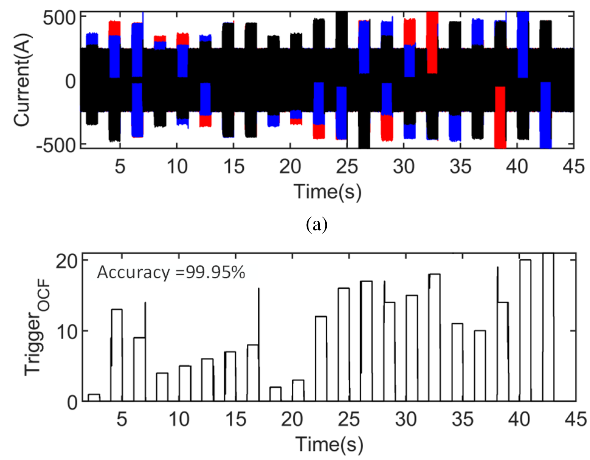

Fig. 26. CHIL OCF diagnosis for all operational states in Table 1. (a) Three-phase current. (b) OCF diagnosis signal.

real-time accuracy dip for different classifiers caused by the misclassifications due to OCF detection latency. The classifier with the highest latency has the highest dip, thus resulting in less overall accuracy, slow diagnosis, probable congestion in the communication network at high RPMs, and false alarms. Therefore, it is important to consider the timing profiles during reliability quantification as in (14) to scale the practical effectiveness of an ML-based approach across MDSs spanning a wide speed range. So, considering the temporal analysis of ML networks and the communication framework, the reliability score for each ML classifier is given in Table 3. Thus, considering the offline validation results and reliability scores, FNN is opted as a reliable ML classifier to further validate the performance of the proposed OCF diagnosis scheme.

F. Real-Time FNN-Based CHIL OCF Diagnosis

In order to further substantiate the practical applicability of the proposed approach, various case study scenarios from Table 1 are implemented via the CHIL experimental setup. The real-time data acquisition results related to the three-phase output current and OCF diagnosis signal are displayed by using an oscilloscope (Tektronix TDS2024 C) connected to the analog output port of OPAL-RT. The CH1, CH2, and CH3 correspond to phase-A, B, and C currents, while CH4 is linked to the fault diagnosis signal obtained via Raspberry Pi.

In this regard, Figs. 23 and 24(a), illustrate two scenarios of SS-OCFs, where there is no phase-A positive current component for OCF in S1 and no negative current component for OCF in S4. Moreover, t_0 represents the time when OCF has been instigated, while t_1 is the time of OCF detection. The fault diagnosis signal shows the associated label value according to Table 1. Furthermore, Fig. 24(b) shows the OCF diagnosis for SDS-OCF in Phase-A and B. Since both the upper and lower switches of phases A and B are under OCF therefore, the current for both phases has become zero. Moreover, the associated fault label, i.e., 7, is also successfully detected. For the scenarios of CDS-OCF and PDS-OCF in Figs. 25(a) and (b), respectively, the OCF in the upper switch reduces the positive current of the associated phase to zero, while the OCF in the lower switch eliminates the negative current of the associated phase. Moreover, the assigned labels to each category of faults are shown as a fault diagnosis signal. Finally, to demonstrate the comprehensive effectiveness of the proposed OCF diagnosis approach, all OCF categories outlined in Table 1 are randomly executed in real-time, as shown in Fig. 26. The classifier shows misclassifications in certain instances, particularly during the transition states. However, during the steady state, the OCFs are perfectly diagnosed. The overall accuracy of the suggested FNN-based classifier, as illustrated in Fig. 26(b), is less than that shown in Table 3, indicating the classifier's sensitivity concerning different operating conditions. Hence, the false alarms caused by the real-world operating conditions associated with MDS can be subdued by using a majority vote mechanism (MVM). In this scheme, the classifier's output is considered for multiple instants after the first trigger, rather than the disturbance trigger for a single instant, reducing the chances of false alarms but also increasing the diagnosis time. So, by adopting the MVM approach, the accuracy of the proposed OCF diagnosis can be further improved.

TABLE IV
COMPARISON OF ML-BASED FAULT DIAGNOSIS METHODS

Type of faults	ML model	Data preprocessing	Window size	Detection time	Accuracy	Computational effort
Single and double -switch OCFs [9]	ELM	PCA	40ms (fixed)	>40ms	96.76%	Medium
Single and double -switch OCFs [22]	HEL	FFT and ReliefF	25ms (fixed)	30ms	99.00%	High
Single and double -switch OCFs, and sensor faults [16]	RVFL	FFT and ReliefF	20ms (fixed)	22ms	98.83%	High
Single and double -switch OCFs [37]	BN	FFT and PCA	—	71ms	98.99%	High
Single and double -switch OCFs [19]	MRVM	FFT and PCA	20ms (fixed)	131ms	98.11%	High
Voltage, current, and speed sensor faults [36]	ELM	None	8ms (fixed)	10ms	98.00%	Low
(Proposed method) Single and double -switch OCFs	**FNN**	**None**	**1 FP**	**1 FP+0.6ms**	**99.95%**	**Low (620 FLOPs)**

ELM (extreme learning model). HEL (hybrid ensemble learning). RVFL (random vector functional link). BN (Bayesian networks). MRVM (multikernel relevance vector machines). FLOPs (floating-point operations). FP (fundamental period).

G. Comparative Analysis With Prior Studies

Finally, Table 4 presents a comparative analysis of the proposed scheme with various previous studies that utilized data-driven approaches for fault diagnosis in power electronic systems. Most existing schemes exhibit one or both of the following limitations: reliance on complex data preprocessing techniques for feature extraction and the use of a fixed feature extraction window size. These shortcomings lead to increased computational demands, insufficient or excessive diagnostic data, and timing overruns, especially in applications with dynamic speed profiles, such as those in the automotive sector. The proposed approach offers significant advantages over existing methods, including independence from preprocessing techniques, a dynamic feature extraction window size of 1 FP, a minimal detection time, and superior accuracy. To assess the computational burden of the proposed FNN, the number of floating-point operations (FLOPs) is quantified, as presented in Table 4. Furthermore, since prior published works lack a detailed architecture of their data-driven schemes, accurately determining their FLOPs values remains challenging.

V. CONCLUSION

This study provides a practically more viable approach for reliability score benchmarking of data-driven schemes used for OCF diagnosis in MDS. Moreover, the conduction loss profiles associated with each semiconductor device in the power converter are proposed as a new system's operational feature extraction approach for OCF diagnosis, reflecting the enhanced applicability of ATM-based schemes. Moreover, these loss profiles further estimated the thermal impact of OCFs on each MOSFET. The proposed approach is validated via the CHIL experiment as well, showing an accuracy of 99.95% for 21 different modes of OCFs. Moreover, the reliability score quantification approach considers real-time timing profiles as a crucial parameter of the system for practical implementation, hence making it a more reliable method for data-driven-based OCF diagnosis system design for power converters.

The proposed OCF diagnosis approach is independent of any system parameters, and it can be extended for a multilevel inverter due to the inherent segregation property of the ATM scheme. In addition, the thermal impact analysis can also be further used for degradation forecasting of healthy switches due to OCFs for a more sophisticated critical time estimation in reliability score quantification, which will be a focus of our future work. Moreover, OCF localization will also be associated with an adaptive fault-tolerant operation to develop a resilient control approach for our upcoming research work.

ACKNOWLEDGMENT

Distribution statement A. Approved for public release; distribution is unlimited. OPSEC8438. The authors would like to express their gratitude for the valuable resources and facilities provided by the Secure Energy and Automation Laboratory (SEAL) and Real Time Controls and Optimization Laboratory (RTCOOL). The authors would like to acknowledge the Warren H. Owen Distinguished Professorship Endowment for its support of the research effort.

REFERENCES

[1] X. Zhou, J. Sun, H. Li, M. Lu, and F. Zeng, "PMSM open-phase fault-tolerant control strategy based on four-leg inverter," *IEEE Trans. Power Electron.*, vol. 35, no. 3, pp. 2799–2808, Mar. 2020.

[2] Z. Gao, C. Cecati, and S. X. Ding, "A survey of fault diagnosis and fault-tolerant techniques—Part i: Fault diagnosis with model-based and signal-based approaches," *IEEE Trans. Ind. Electron.*, vol. 62, no. 6, pp. 3757–3767, Jun. 2015.

[3] S. Zhuo, A. Gaillard, L. Xu, C. Liu, D. Paire, and F. Gao, "An observer-based switch open-circuit fault diagnosis of dc–dc converter for fuel cell application," *IEEE Trans. Ind. Appl.*, vol. 56, no. 3, pp. 3159–3167, May/Jun. 2020.

[4] N. Wassinger, E. Penovi, R. G. Retegui, and S. Maestri, "Open-circuit fault identification method for interleaved converters based on time-domain analysis of the state observer residual," *IEEE Trans. Power Electron.*, vol. 34, no. 4, pp. 3740–3749, Apr. 2019.

[5] Y. Yu, Y. Zhao, B. Wang, X. Huang, and D. Xu, "Current sensor fault diagnosis and tolerant control for VSI-based induction motor drives," *IEEE Trans. Power Electron.*, vol. 33, no. 5, pp. 4238–4248, May 2018.

[6] W. Hwang and K. Huh, “Fault detection and estimation for electromechanical brake systems using parity space approach,” *J. Dynamic Syst., Measurement, Control*, vol. 137, no. 1, p. 0 14504, 2015.

[7] J. Poon, P. Jain, I. C. Konstantakopoulos, C. Spanos, S. K. Panda, and S. R. Sanders, “Model-based fault detection and identification for switching power converters,” *IEEE Trans. Power Electron.*, vol. 32, no. 2, pp. 1419–1430, Feb. 2017.

[8] D. Xie and X. Ge, “A state estimator-based approach for open-circuit fault diagnosis in single-phase cascaded H-bridge rectifiers,” *IEEE Trans. Ind. Appl.*, vol. 55, no. 2, pp. 1608–1618, Mar./Apr. 2019.

[9] Y. Xia and Y. Xu, “A transferrable data-driven method for IGBT open-circuit fault diagnosis in three-phase inverters,” *IEEE Trans. Power Electron.*, vol. 36, no. 12, pp. 13478–13488, Dec. 2021.

[10] Z. Liu, L. Fang, D. Jiang, and R. Qu, “A machine-learning-based fault diagnosis method with adaptive secondary sampling for multiphase drive systems,” *IEEE Trans. Power Electron.*, vol. 37, no. 8, pp. 8767–8772, Aug. 2022.

[11] H. Zhao and L. Cheng, “Open-switch fault-diagnostic method for back-to-back converters of a doubly fed wind power generation system,” *IEEE Trans. Power Electron.*, vol. 33, no. 4, pp. 3452–3461, Apr. 2018.

[12] B. Gou, X.-L. Ge, Y.-C. Liu, and X.-Y. Feng, “Load-current-based current sensor fault diagnosis and tolerant control scheme for traction inverters,” *Electron. Lett.*, vol. 52, no. 20, pp. 1717–1719, 2016.

[13] D. Zhou, H. Qiu, S. Yang, and Y. Tang, “Submodule voltage similarity-based open-circuit fault diagnosis for modular multilevel converters,” *IEEE Trans. Power Electron.*, vol. 34, no. 8, pp. 8008–8016, Aug. 2019.

[14] D. Zhou, S. Yang, and Y. Tang, “A voltage-based open-circuit fault detection and isolation approach for modular multilevel converters with model-predictive control,” *IEEE Trans. Power Electron.*, vol. 33, no. 11, pp. 9866–9874, Nov. 2018.

[15] S. Khojet El Khil, I. Jlassi, A. J. Marques Cardoso, J. O. Estima, and N. Mrabet-Bellaaj, “Diagnosis of open-switch and current sensor faults in PMSM drives through stator current analysis,” *IEEE Trans. Ind. Appl.*, vol. 55, no. 6, pp. 5925–5937, Nov./Dec. 2019.

[16] B. Gou, Y. Xu, Y. Xia, Q. Deng, and X. Ge, “An online data-driven method for simultaneous diagnosis of IGBT and current sensor fault of three-phase PWM inverter in induction motor drives,” *IEEE Trans. Power Electron.*, vol. 35, no. 12, pp. 13281–13294, Dec. 2020.

[17] G. Zhiwei et al., “A survey of fault diagnosis and fault-tolerant techniques—Part ii: Fault diagnosis with knowledge-based and hybrid/active approaches,” *IEEE Trans. Indus. Electron.*, vol. 62, no. 6, pp. 3768–3774, Jun. 2015.

[18] B. Cai, Y. Zhao, H. Liu, and M. Xie, “A data-driven fault diagnosis methodology in three-phase inverters for PMSM drive systems,” *IEEE Trans. Power Electron.*, vol. 32, no. 7, pp. 5590–5600, Jul. 2017.

[19] T. Wang, H. Xu, J. Han, E. Elbouchikhi, and M. E. H. Benbouzid, “Cascaded h-bridge multilevel inverter system fault diagnosis using a PCA and multiclass relevance vector machine approach,” *IEEE Trans. Power Electron.*, vol. 30, no. 12, pp. 7006–7018, Dec. 2015.

[20] S. Ye, J. Jiang, J. Li, Y. Liu, Z. Zhou, and C. Liu, “Fault diagnosis and tolerance control of five-level nested NPP converter using wavelet packet and LSTM,” *IEEE Trans. Power Electron.*, vol. 35, no. 2, pp. 1907–1921, Feb. 2020.

[21] Z. Xue, K. Xiahou, M. Li, T. Ji, and Q. Wu, “Diagnosis of multiple open-circuit switch faults based on long short-term memory network for DFIG-based wind turbine systems,” *IEEE Trans. Emerg. Sel. Topics Power Electron.*, vol. 8, no. 3, pp. 2600–2610, Sep. 2020.

[22] Y. Xia, Y. Xu, and B. Gou, “A data-driven method for IGBT open-circuit fault diagnosis based on hybrid ensemble learning and sliding-window classification,” *IEEE Trans. Ind. Inform.*, vol. 16, no. 8, pp. 5223–5233, Aug. 2020.

[23] S. U. Jan, Y.-D. Lee, J. Shin, and I. Koo, “Sensor fault classification based on support vector machine and statistical time-domain features,” *IEEE Access*, vol. 5, pp. 8682–8690, 2017.

[24] A. Arsalan et al., “Cyber attack detection and classification for integrated on-board electric vehicle chargers subject to stochastic charging coordination,” *Transp. Res. Procedia*, vol. 70, pp. 44–51, 2023.

[25] L. Wen, X. Li, L. Gao, and Y. Zhang, “A new convolutional neural network-based data-driven fault diagnosis method,” *IEEE Trans. Ind. Electron.*, vol. 65, no. 7, pp. 5990–5998, Jul. 2018.

[26] S.-H. Kim, D.-Y. Yoo, S.-W. An, Y.-S. Park, J.-W. Lee, and K.-B. Lee, “Fault detection method using a convolution neural network for hybrid active neutral-point clamped inverters,” *IEEE Access*, vol. 8, pp. 140632–140642, 2020.

[27] A. Moradzadeh, B. Mohammadi-Ivatloo, K. Pourhossein, and A. Anvari-Moghaddam, “Data mining applications to fault diagnosis in power electronic systems: A systematic review,” *IEEE Trans. Power Electron.*, vol. 37, no. 5, pp. 6026–6050, May 2022.

[28] T. Shi, Y. He, T. Wang, and B. Li, “Open switch fault diagnosis method for PWM voltage source rectifier based on deep learning approach,” *IEEE Access*, vol. 7, pp. 66595–66608, 2019.

[29] G. Ozkan, P. H. Hoang, P. R. Badr, C. S. Edrington, and B. Papari, “Real-time thermal management for two-level active rectifier with finite control set model predictive control,” *Int. J. Elect. Power Energy Syst.*, vol. 131, 2021, Art. no. 107057.

[30] CREE Wolfspeed, “CAB530M12BM3 datasheet,” *Datasheet*, 2021. [Online]. Available: https://assets.wolfspeed.com/uploads/2021/05/CAB530M12BM3

[31] A. Arsalan et al., “Machine learning approach for open circuit fault detection and localization in EV motor drive systems,” SAE Tech. Paper, Tech. Rep., 2024.

[32] M. Sokolova and G. Lapalme, “A systematic analysis of performance measures for classification tasks,” *Inform. Process. Manage.*, vol. 45, no. 4, pp. 427–437, 2009.

[33] S. Hochreiter and J. Schmidhuber, “Long short-term memory,” *Neural Comput.*, vol. 9, no. 8, pp. 1735–1780, 1997.

[34] S. Dusmez, H. Duran, and B. Akin, “Remaining useful lifetime estimation for thermally stressed power mosfets based on on-state resistance variation,” *IEEE Trans. Ind. Appl.*, vol. 52, no. 3, pp. 2554–2563, May/Jun. 2016.

[35] A. Nordelöf, E. Grunditz, S. Lundmark, A.-M. Tillman, M. Alatalo, and T. Thiringer, “Life cycle assessment of permanent magnet electric traction motors,” *Transp. Res. Part D: Transport Environ.*, vol. 67, pp. 263–274, 2019.

[36] B. Gou, Y. Xu, Y. Xia, G. Wilson, and S. Liu, “An intelligent time-adaptive data-driven method for sensor fault diagnosis in induction motor drive system,” *IEEE Trans. Ind. Electron.*, vol. 66, no. 12, pp. 9817–9827, Dec. 2019.

[37] B. Cai, Y. Zhao, H. Liu, and M. Xie, “A data-driven fault diagnosis methodology in three-phase inverters for PMSM drive systems,” *IEEE Trans. Power Electron.*, vol. 32, no. 7, pp. 5590–5600, Jul. 2017.

Ali Arsalan (Graduate Student Member, IEEE) received the master’s degree in electrical engineering from UET, Lahore, Pakistan, in 2019. He is currently working toward the Ph.D. degree in automotive engineering. with the Department of Automotive Engineering, International Center for Automotive Research, Clemson University, Clemson, SC, USA.

From 2017 to 2022, he was a Laboratory Engineer with the Khwaja Fareed University of Engineering and Information Technology, Rahim Yar Khan, Pakistan. He is a Graduate Research Assistant with Secure Energy and Automation Laboratory, International Center for Automotive Research, and Real-Time COntrol and Optimization Laboratory, Electrical and Computer Engineering, Clemson University. His research interests include automotive cybersecurity, machine learning, power electronics, electric drive systems, optimization, microgrids, and energy management.

Behnaz Papari (Senior Member, IEEE) received the B.S. degree from the University of Bushehr, Bushehr, Iran, in 2008, and the M.Sc. degree from the K. N. Toosi University of Technology, Tehran, Iran, in 2011, both in electrical engineering, and the Ph.D. degree in electrical and computer engineering from Florida State University, Tallahassee, FL, USA, in 2018.

Prior to joining the Department of Automotive Engineering and Electrical and Computer Engineering, Clemson University, in Spring 2022, she was an Assistant Professor with the Department of Marine Engineering Technology, Texas A&M University, College Station, TX, USA, and an Assistant Professor of practice with the Energy Production and Infrastructure Center, University of North Carolina at Charlotte, Charlotte, NC, USA, for three years, where she taught at undergraduate and graduate levels. Her background is in power systems controls, with an emphasis on modeling, analysis, planning, and AI-based optimization. Her research interests include distributed controls and secure control frameworks under uncertainty, applications on energy system modeling, stochastic optimization, and electric vehicles, including electric and hybrid-electric and ESSs.

Laxman Timilsina (Member, IEEE) received the B.E. degree in electrical engineering from the Institute of Engineering, Tribhuvan University, Kathmandu, Nepal, in 2016, the M.Sc. degree in distributed generation in electrical engineering from Tribhuvan University, Kathmandu, Nepal, in 2019, and the Ph.D. degree in electrical engineering from Clemson University, Clemson, SC, USA, in May 2024, under the mentorship of Dr. Christopher S. Edrington.

Concurrently, he was a Graduate Research Assistant with the Real-Time Control and Optimization Laboratory (RT-COOL), The Holcombe Department of Electrical and Computer Engineering (ECE), Clemson University. He is currently a Postdoctoral Researcher Fellow with RTCOOL. His research interests include electrified vehicles, integration of renewable energy, ship power systems, and smart grids.

Grace Muriithi (Graduate Student Member, IEEE) received the B.Sc. degree from Jomo Kenyatta University of Agriculture and Technology, Juja, Kenya, and the M.Sc. degree from the University of Cape Town, Cape Town, South Africa, in 2018 and 2022, respectively, both in electrical engineering. She is currently working toward the Ph.D. degree in automotive engineering with Clemson University's International Centre for Automotive Research, Clemson, SC, USA, specializes in enhancing the resilience and security of cyber–physical systems.

Her research focuses on hybrid electric vehicles and electric vehicle charging stations. Her research interests include cyber–physical systems security, machine learning, energy management, power systems, and vulnerability analysis in advanced control systems. Grace's work contributes to the critical field of automotive cybersecurity in an increasingly electrified and connected transportation landscape.

Ali Moghassemi (Graduate Student Member, IEEE) received the B.S. and M.S. degrees in electrical engineering from Islamic Azad University, South Tehran Branch, Tehran, Iran, in 2012 and 2015, respectively. He is currently working toward the Ph.D. degree in electrical and computer engineering with Clemson University, Clemson, SC, USA.

He has authored and coauthored several peer-reviewed papers in journals and conferences, two book chapters, and one book. His research interests include modeling, simulation, and control of renewable energy systems, partially shaded photovoltaics, power electronics, z-source inverters, power quality, dynamic voltage restorer, and voltage disturbances. His areas of interest include renewable energy systems, power electronics, and power quality.

Dr. Moghassemi has been serving as a Reviewer for several scientific journals over the years.

SM Imrat Rahman (Graduate Student Member, IEEE) received the B.Sc. degree in electrical and electronic engineering from the Islamic University of Technology, Gazipur, Bangladesh, in 2010, and the M.Sc. degree in power engineering from the Technical University of Munich, Munich, Germany, in 2015. He is currently working toward the Ph.D. degree in electrical and computer engineering with the Holcombe Department of Electrical and Computer Engineering, Clemson University, Clemson, SC, USA, under the supervision of Dr. Christopher S. Edrington and Dr. Gokhan Ozkan.

He was a Lecturer with American International University-Bangladesh, Dhaka, Bangladesh. He is currently a Graduate Research Assistant with Real-Time Control and Optimization Laboratory, Clemson University. His research interests include active thermal management of power electronic converters, distributed control, and thermal modeling of power electronic building blocks systems.

Elutunji Buraimoh (Graduate Student Member, IEEE) received the B.Tech. (Hons.) degree from the Ladoke Akintola University of Technology, Ogbomosho, Nigeria, and the M.Sc. degree from Obafemi Awolowo University, Ife, Nigeria, in 2012 and 2016, respectively, both in electronic and electrical engineering, the D.Eng. degree in power engineering from the Durban University of Technology, Durban, South Africa, in 2021, and the Ph.D. degree in electrical and computer engineering from Clemson University, Clemson, SC, USA, in 2025.

He is a registered Engineer of the Council for the Regulation of Engineering in Nigeria, Abuja, Nigeria, and a Candidate for the Engineering Council of South Africa, Johannesburg, South Africa. His previous studies focused on microgrids, renewable energy, power systems control, and FACTS devices. His research interests include geographically distributed real-time co-simulation of power systems, communication latency compensation, and energy management.

Dr. Buraimoh is a Corporate Member of the NSE, and a Member of SAE.

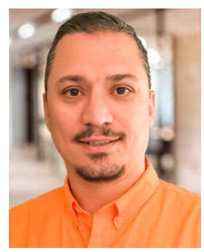

Gokhan Ozkan (Senior Member, IEEE) received the B.Sc. degree in electric education from Marmara University, Istanbul, Turkey, in 2006, the B.Sc. (as a Valedictorian) and M.Sc. degrees in energy systems engineering from Erciyes University, Kayseri, Turkey, in 2014 and 2016, respectively, and the Ph.D. degree in electrical engineering from Florida State University, Tallahassee, FL, USA, in 2019.

In 2020, he was a Postdoctoral Fellow with Clemson University, Clemson, SC, USA. Since 2021, he has been a Research Assistant Professor with The Holcombe Department of Electrical and Computer Engineering, Clemson University. He is currently the Research Lead with the Energy Innovation Center, North Charleston, SC, USA, and also the Manager of the Real-Time COntrol and Optimization Laboratory. His research interests include power systems and DER integration, model predictive control in power converters and drives, active thermal management and fault-tolerant control, distributed controls, power and EM, real-time power distribution system modeling, simulation, co-simulations, and hardware-in-the-loop instantiation.

Christopher S. Edrington (Senior Member, IEEE) received the B.S. degree in engineering from Arkansas State University, Jonesboro, AR, USA, in 1999, and the M.S. and Ph.D. degrees in electrical engineering from the Missouri University of Science and Technology, Rolla, MO, USA, in 2001 and 2004, respectively.

He was both a GAANN and IGERT Fellow of Missouri University of Science and Technology. From 2004 to 2007, he was an Assistant Professor in electrical engineering with the College of Engineering, Arkansas State University. From 2007 to 2019, he was an Assistant Professor, an Associate Professor, and a Full Professor in electrical and computer engineering with the FAMU-FSU College of Engineering and was the Lead of the Energy Conversion and Integration Thrust, Center for Advanced Power Systems, Florida State University, Tallahassee, FL, USA. In 2019, he was the Warren H. Owen Distinguished Professor of electrical and computer engineering with Clemson University, Clemson, SC, USA, where he leads the Real-Time COntrol and Optimization Laboratory. He is currently the Associate Director of industry relations with the VIPR-GS Center, Clemson University. His research interests include modeling, simulation, optimization, and control of electromechanical drive systems, applied power electronics, integration of renewable energy, storage, pulse power loads, and hardware in the loop VV&A experimentation.